

Oxidation of nanopores in a silicon membrane: self-limiting formation of sub-10 nm circular openings

This content has been downloaded from IOPscience. Please scroll down to see the full text.

2014 Nanotechnology 25 355302

(<http://iopscience.iop.org/0957-4484/25/35/355302>)

View [the table of contents for this issue](#), or go to the [journal homepage](#) for more

Download details:

IP Address: 130.237.214.51

This content was downloaded on 13/08/2014 at 13:56

Please note that [terms and conditions apply](#).

Oxidation of nanopores in a silicon membrane: self-limiting formation of sub-10nm circular openings

Miao Zhang¹, Torsten Schmidt¹, Fatemeh Sanghaleh¹, Niclas Roxhed², Ilya Sychugov¹ and Jan Linnros¹

¹Materials and Nano Physics, School of Information and Communication Technology, KTH Royal Institute of Technology, Electrum 229, SE-16440 Kista-Stockholm, Sweden

²Micro and Nanosystems, School of Electrical Engineering, KTH Royal Institute of Technology, Osquldas Väg 10, SE-10044 Stockholm, Sweden

E-mail: miaoz@kth.se

Received 2 May 2014, revised 17 June 2014

Accepted for publication 8 July 2014

Published 12 August 2014

Abstract

We describe a simple but reliable approach to shrink silicon nanopores with nanometer precision for potential high throughput biomolecular sensing and parallel DNA sequencing. Here, nanopore arrays on silicon membranes were fabricated by a self-limiting shrinkage of inverted pyramidal pores using dry thermal oxidation at 850 °C. The shrinkage rate of the pores with various initial sizes saturated after 4 h of oxidation. In the saturation regime, the shrinkage rate is within $\pm 2 \text{ nm h}^{-1}$. Oxidized pores with an average diameter of 32 nm were obtained with perfect circular shape. By careful design of the initial pore size, nanopores with diameters as small as 8 nm have been observed. Statistics of the pore width show that the shrinkage process did not broaden the pore size distribution; in most cases the distribution even decreased slightly. The progression of the oxidation and the deformation of the oxide around the pores were characterized by focused ion beam and electron microscopy. Cross-sectional imaging of the pores suggests that the initial inverted pyramidal geometry is most likely the determining factor for the self-limiting shrinkage.

Keywords: solid-state nanopores, silicon, thermal oxidation

(Some figures may appear in colour only in the online journal)

Introduction

Nanopore-based molecular translocation and sensing has become a rapidly expanding research field since the 1990s when reading the DNA sequence using a nanopore whose diameter is comparable to the width of a single DNA strand was proposed and demonstrated on the 1.5 nm biological pore α -hemolysin [1, 2]. The vast follow-up research has shown that not just the sequence of the nucleotides of DNA or RNA, but also various properties of the biomolecules, such as the length of DNA or RNA and the size and shape of proteins, can be studied directly by measuring the ionic current change or the optical signal when a molecule passes through a nanopore [3–7]. In fact, because of the fast translocation of

molecules through a nanopore and the potential to scale up from a single pore to an array of pores, nanopore-based sensing or sequencing is believed to have a very high throughput which is crucial in biotechnology applications. The high expectation of realizing these ideas into applications has driven a major research effort focused on fabrication of solid-state pores, due to their obvious advantages over biological protein pores, including mechanical stability, chemical inertness, controllable diameter, and compatibility with semiconductor technology. The latter especially allows solid-state nanopores to be potentially integrated with semiconductor devices and scaled up to large arrays. So far, various methods to fabricate nanopores in solid-state materials have been demonstrated. For membranes made of

semiconductor fabrication-compatible materials, the first nanopores with diameters comparable to biological pores, 1.8 nm, have been etched in SiN membranes by using a customized focused ion beam (FIB) with a feedback control [8]. Later, cylindrical pores have been ‘drilled’ and shrunk with nanometer precision in thin SiO₂ and SiN membranes using a focused electron beam in commercially available transmission electron microscopes (TEM) [9–11]. More economical approaches to obtain nanopores employing wet chemistry etching have also been reported. Sub-10 nm pores can be formed in Si membranes by anisotropic etching of Si in an alkaline solution, such as KOH, with a current feedback system [12]. In polymer membranes, conical pores with diameters as small as 2 nm can be created by chemical etching of the latent track of single energetic heavy ions [13]. These methods are, however, restricted to the fabrication of single nanopores or to pores within small array sizes, because the fabrication processes are time consuming and only allow pores to be made one by one.

Given the motivation to use nanopores for high throughput biomolecular sensing/sequencing, a rapid fabrication method of nanopores in a large array is of particular interest. Several attempts to make nanopores in a large array have been reported. Bashir’s group has shown nanopores shrunk to about 15 nm in diameter with a pitch distance of 105 nm by atomic layer deposition in anodized aluminum oxide (AAO) membranes [14]. However, this method is restricted to the AAO template where the pitch distance between pores cannot be adjusted and therefore pores are too close for parallel sensing using any optical readout approach. Electrochemical etching of a pre-patterned silicon membrane has also been employed to fabricate nanopores with high aspect ratio and controlled pitch distances [15, 16]. So far, the minimal diameter of electrochemically etched pores is about 30 nm, which is still too large for single molecule sensing or DNA sequencing. More recently, Deng *et al* demonstrated a simple method to shrink inverted pyramidal silicon pores by thermal oxidation to obtain nanopores [17]. In fact, oxidation of silicon is a highly reliable process with nanometer precision, which has been intensively studied and developed since the 1960s to fabricate ultrathin gate oxide layers for semiconductor transistors. Especially, the stress-related oxidation or self-limiting oxidation on non-planar silicon structures has been elucidated and utilized on purpose to fabricate silicon nanowires with sub-5 nm diameters, single electron transistors, and arrays of single silicon quantum dots [18–23]. In Deng *et al*’s work, nanopores with diameters about 30 nm were fabricated in a 4 by 3 array. However, for high throughput biomolecular sensing/sequencing applications, the size of the oxidized pores needs to be further reduced and the array size enlarged. This raises the question, namely to what extent the variation of the oxidation shrinking process influences the final pore size distribution at a large scale. Moreover, the progression and the mechanism of oxidation of complex 3-dimensional silicon structures require a careful investigation and clear elucidation of the involved processes. These would allow us to benefit from the well-accumulated knowledge of silicon oxidation, to further improve the

oxidation of silicon as a nanopore shrinking technique with true nanometer precision.

To answer these questions, aiming at high throughput parallel DNA sequencing, we present a simple but reliable method to fabricate nanopores in a large array on a silicon-on-insulator (SOI) wafer by standard cleanroom processing, including lithography, dry and wet etching, and thermal oxidation. The membranes are several hundred nanometers thick and mechanically robust. The pitch distance and the array size are controlled by lithography, and thus are adjustable and not limited in dimension. Interestingly, a self-limiting behavior of the pore shrinking process during thermal oxidation was found on pores with various initial sizes, which has not been reported before. With the self-limiting shrinkage effect, circular pores with a diameter as small as 8 nm have been formed by thermal oxidation. Pore size distributions were examined on 400 pores through the oxidation process. By using FIB and TEM, the oxidation progression of the silicon pores and the self-limiting shrinkage effect were studied. In addition, the inner pore structure has been characterized and analyzed with regard to potential applications.

Experimental details

Membranes, 100 by 100 μm², were fabricated by optical lithography and inductively coupled plasma (ICP) etching on the backside of an SOI wafer (p-type (100), SOITEC) using the Bosch process. A 10 μm thick resist (AZ9260, AZ Electronic Materials) was used as a soft mask during the backside etching process. The suspended membranes consisted of a 400 nm buried oxide layer, a 300 nm silicon (device) layer and 100 nm silicon dioxide on top. Then, arrays of squares were defined on the front side of the membranes by either optical or e-beam lithography using positive resists (PMMA or Zep520, respectively). By reactive ion etching, the pattern was transferred to the oxide top layer, which acted as a hard mask for the following wet etching step. Inverted truncated pyramids were formed by anisotropic etching of the silicon membranes in 30% KOH at 80 °C for 90 s. Finally, oxide layers on both sides of the silicon membranes were removed in 5% HF, leaving free-standing silicon membranes with arrays of truncated rectangular pyramidal pores.

Oxidation of the as-prepared membranes was carried out in a dry O₂ atmosphere at 850 °C (Thermco furnace model 5200, Thermco System) for different time periods up to 10 h. This temperature was chosen in consideration of the relatively slow oxidation rate and the high viscosity of the SiO₂ at 850 °C to possibly obtain self-limiting oxidation and to gain better control over the shrinkage process. The furnace was held at a standby temperature of 625 °C with a N₂ atmosphere. After the samples were loaded into the furnace, the temperature was ramped up at a rate of 8 °C min⁻¹. When the temperature reached the set point, O₂ atmosphere was established at about 1 atm. After oxidation, the furnace was ramped down to 625 °C at a rate of 4 °C min⁻¹. Before each step of oxidation, the samples were cleaned with oxygen plasma and

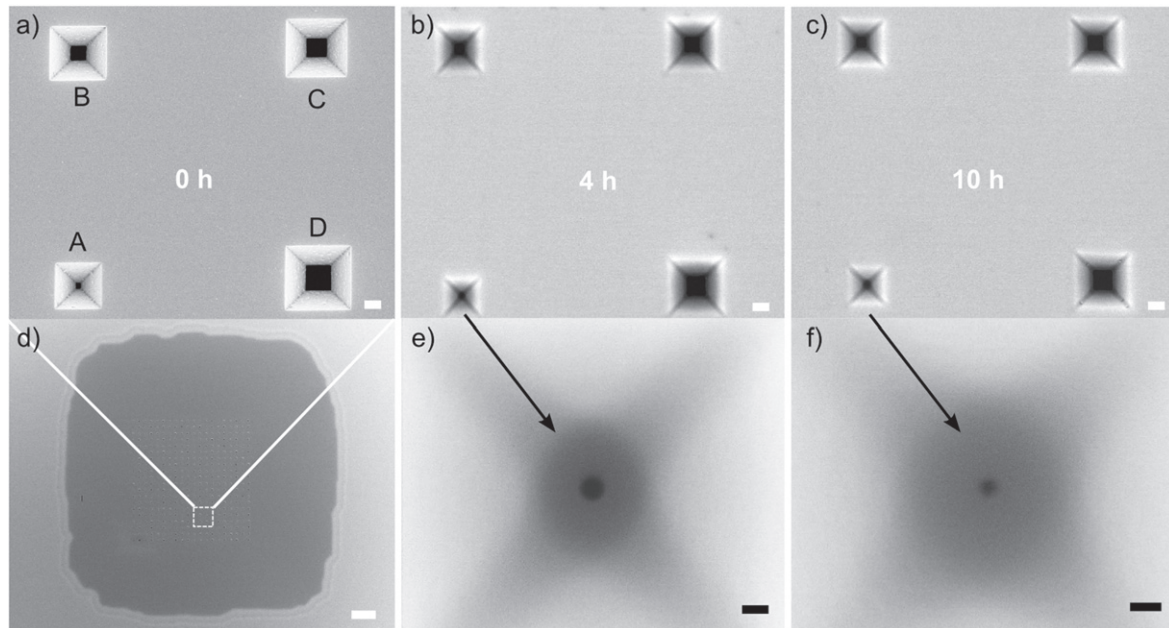


Figure 1. Upper panel: (a)–(c) series of SEM top view images showing successive oxidation steps, before and after 4 and 10 h, respectively. Each of the micrographs depicts the same unit which contains four pyramidal pores with different initial sizes, marked with A, B, C, and D. Lower panel: (d) arranged in an array of 10 by 10, these 4 pore units are located in the central part of the silicon membrane. The unit shown in the upper panel is indicated by the dashed white square. (e) and (f) Zoomed-in images of the pore labeled as A after 4 and 10 h of oxidation showing circular pores with diameters of 11 nm and 8 nm, respectively. The scale bars are 200 nm (a)–(c), 10 μm (d), and 20 nm (e), (f), respectively.

acetone to remove carbon contamination resulting from scanning electron microscope inspections.

The progress of the oxidation, i.e. the shrinkage of the pores, was characterized by scanning electron microscopy (SEM: Gemini, ULTRA 55, Zeiss) and TEM (JEM 2100F (HR), JEOL Electron Microscope 2100 Field, JEOL). The software ImageJ was used to process batches of images to measure pore size distributions. Digital Micrograph was used to analyze the TEM images. Furthermore, to study the effect of the oxidation in detail, cross-sectional samples, revealing the shape of the nanopores, were prepared by using FIB (QUANTA 3D FEG, FEI). To do so, platinum was routinely deposited on the area of interest to protect the sample from ion milling. Then, for TEM imaging, a lamella was carefully cut off from the membrane and transferred to a separate copper mesh. The platinum deposition into the nanopores enhanced the contrast between the oxide and the hollow nanopores, which allowed observation of nanopores with diameters of less than 20 nm embedded in over 100 nm thick oxide. With the precision of FIB, individual pores could be selected and thus both characterization in top view and cross section are accessible for the same pore.

Results and discussion

A set of typical SEM top view images of a silicon membrane is shown in figure 1. Pores with different dimensions (labeled with A, B, C, and D) with a pitch distance of 2 μm were designed as a unit (see figure 1(a)). On one membrane, there

are 10 by 10 such units with the same pitch distance of 2 μm (see figure 1(d)). In other words, 100 pores of each size group were evenly distributed across the membrane. This specific arrangement is used to study the oxidation of pores with different initial sizes with minimized influence from local variations across the membrane on the oxidation and shrinkage rate. Such variations might be given by the material itself, e.g. wafer dopant (distribution), or introduced during processing, e.g. proximity effects in lithography, membrane geometry (bulging), etc. Since converting Si into SiO₂ has a volume expansion of 225%, with increasing oxidation time the newly grown oxide pushes out the old oxide, forcing it to rearrange according to the 3-dimensional structure of the silicon, resulting in shrinkage of the pore. Figures 1(a)–(c) show the same unit of four rectangular pores with different initial sizes before (a) and after oxidation ((b) and (c)). As can be observed, in the course of oxidation, initially square-shaped pores with sharp corners become smaller with smooth round corners due to the oxide growth. In particular, the smallest rectangular opening marked as A in figure 1(a) eventually turns into a circular pore, as can be seen in the images of figures 1(e) and (f). In fact, 11 out of 100 larger pores in group A, with initial widths ranging from 58 to 110 nm, remain open after 10 h of oxidation. In fact, all of these end up with perfect circular shape, even the rectangular ones with initial length to width ratios of up to 1.5 prior to oxidation. This is unexpected since the oxidation was carried out at 850 °C, which is much lower than the commonly known glass transition temperature of SiO₂ (965 °C) [24]. To explain this, we need to consider SiO₂ in a plastic flow

regime, which can be described by a shear-dependent viscosity $\eta(\tau)$ [25–28]:

$$\eta(\tau) = \eta_0(T) \frac{\tau/\sigma_c}{\sinh(\tau/\sigma_c)}$$

where $\eta_0(T)$ is the low-stress viscosity at temperature T , τ is the critical resolved shear stress and σ_c is the critical stress threshold where plasticity flow should appear. When the oxide is under high shear stress, it becomes more fluidic. Based on the analysis on concave cylinder structures [25], shear stress increases with curvature. Intuitively, corners of an inverted square pyramidal structure have very large negative curvatures, thus experiencing high shear stress. Hence, the viscosity of the oxide at the corners is lower than the oxide viscosity under low stress, e.g. on a planar structure. This means that oxide in such areas would flow more easily. A smooth shape is naturally preferred by the oxide flow because of its lower surface energy. For the initially small pores, corners are closer to each other, thus the oxide flow merges and forms a circular shape to obtain the lowest surface energy.

In figure 2(a) the average size of all four pore groups is plotted as a function of oxidation time. The data was acquired by recording SEM images of all pores after each oxidation step and measuring their sizes. The average initial size of the pores labelled with A, B, C, and D in figure 1 was measured to be 78 nm, 186 nm, 251 nm, and 312 nm, respectively. Note that for group A only the 11% pores which remained open after 10 h of oxidation were taken into account. With ongoing oxidation time, the shrinkage rate of all four groups of pores slowed down significantly and then saturated after 4 h of oxidation. Moreover, the pore width even slightly increased in a reverse manner from 6 to 10 h. The shrinkage rate in the saturation regime (4 to 10 h) is within a range of $\pm 2 \text{ nm h}^{-1}$, which gives this pore shrinkage method a nanometer precision. The green dashed curve highlights the effect of oxidation for a specific pore, which is also shown in figures 1(e) and (f). Here, a pore with diameter as small as 8 nm was observed after 10 h of oxidation. Remarkably, the saturation of the shrinkage is independent of the initial size. Thus, by reducing the initial size, pores with diameters even smaller than 8 nm would be possible to realize by this process of oxidation, although potentially at an even lower yield.

Figures 2(b) and (c) show typical size distributions of pores before and after oxidation. The plot in figure 2(b) represents group D (black curve D in figure 2(a)) and the plot in figure 2(c) refers to group A (magenta-colored curve A in figure 2(a)). The histograms illustrate that the size distribution of the pores slightly decreases during the oxidation. This means that using oxidation as a method to shrink pores, even below 50 nm, does not enlarge the resulting size variation of the fabrication process. In most cases, it even reduces the size distribution. The spread in the pore size (FWHM: $\sim 40 \text{ nm}$) shown in the histogram was introduced mainly by the lithography and pattern-transfer steps before oxidation and can be further refined.

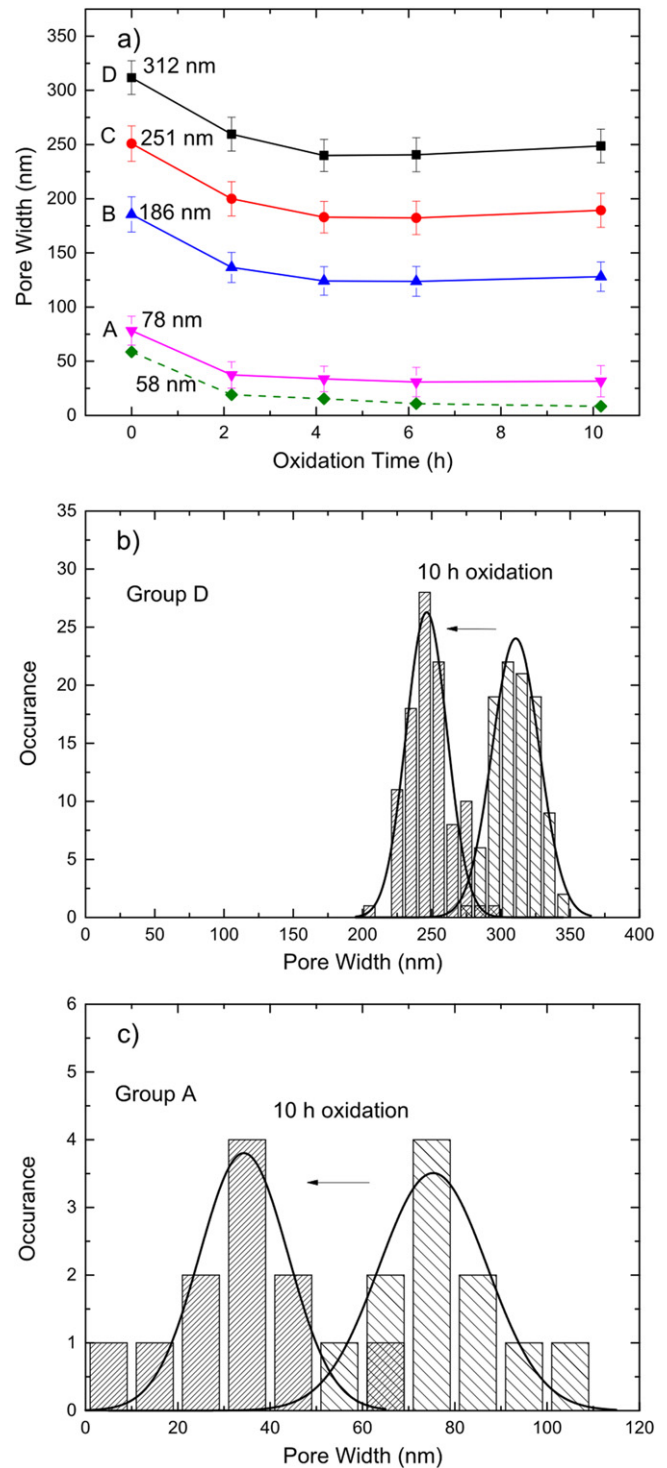


Figure 2. (a) Shrinkage of the pore width as a function of oxidation time. A, B, C, and D are four groups of pores with different initial pore sizes. The dashed line shows the shrinkage of the pore shown in figures 1(e) and (f) with an initial pore width of 58 nm. The error bars represent the standard deviation of the pore widths. (b) and (c) Distributions of the pore width before and after 10 h of oxidation. (b) shows all pores of group D while (c) shows only the fraction of pores of group A which remain open after 10 h of oxidation. For illustration purposes, the histograms are fitted with Gaussian distributions.

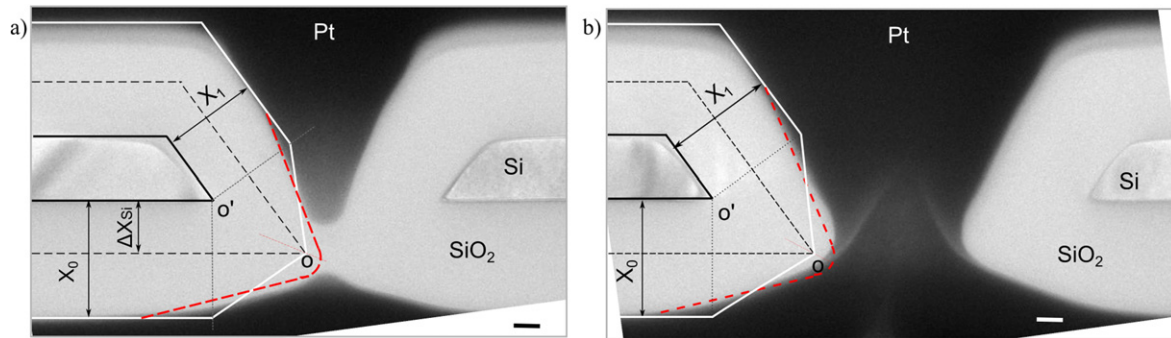


Figure 3. TEM images showing the cross sections of individual pores after 10 h of oxidation cut off by FIB. (a) A pore from group A with an average initial width of 78 nm. (b) A pore from group D with an average initial width of 312 nm. The overlaid schematics on the left side of the images show the volume conversion from Si to SiO₂ and deformation of the SiO₂ at the pore tips. The inner wall oxide (X_1) grows thicker in the pore with larger initial pore size. The dashed black line indicates the initial inverted-pyramidal silicon opening. The solid black line indicates the remaining silicon core after oxidation. The white line illustrates the SiO₂ based on geometric volume expansion. The dashed red line shows SiO₂ deformation at the bottleneck of the pores based on volume conservation. The scale bars in (a) and (b) are 50 nm.

Figure 3 shows an example of a cross-sectional comparison between the smallest (a) and largest (b) initial pore. After 10 h of oxidation, a lamella, about 120 nm thick, containing the very central parts of several pores in a row, was cut off by FIB from the silicon membrane. By examining the lamella in TEM, the cross sections clearly reveal the remaining silicon core, the oxide grown in 10 h of oxidation and the platinum deposition, which is not only covering both sides of the membrane, but also the inside of the pores. Note that the pore in the cross-sectional image (a) became closed during oxidation since its initial size was too small. The left side of the TEM image is overlaid with a schematic to illustrate the geometrical evolution of the pores. The black dashed lines indicate the initial truncated pyramidal pores in silicon with an angle of 54.7°, defined by the KOH etch which has a large selectivity between the Si (100) and (111) plane. By comparing the initial bottom edge of the Si pore with the shape of the oxidized pore, the pore shrinkage can be deduced. In order to obtain better control of the shrinkage process, it is important to understand the relation between oxide growth and shrinkage rate in this geometry.

As Deng *et al* [17] suggested, the shrinkage of the inverted pyramidal pores can be divided into two parts for simplicity: oxide growth based on volume conversion (shown by white lines, $X_0 = 2.25 \Delta X_{Si}$) and oxide deformation according to the geometry needed to achieve a lower surface energy (shown by red dashed lines). Here, assuming SiO₂ is incompressible, the deformation is caused by the rearrangement of oxide based on volume conservation. As shown in figure 3, after 10 h of oxidation, the oxide thickness on the planar part (X_0) is the same along the membrane. However, the oxide grown on the inner walls (X_1) of the pore with smaller initial size from group A is 10% less than that of the pore with larger initial size from group D (X_1 in 3(a) < X_1 in 3(b)). This can be understood by using the stress-related retardation in oxidation of non-planar silicon structures. The oxidation induces compressive stress on concave structures and tensile stress on convex structures, both making oxidation reaction at the interface and diffusion of the oxidant through the oxide more difficult, thus hindering the oxidation [25, 26, 29]. In our

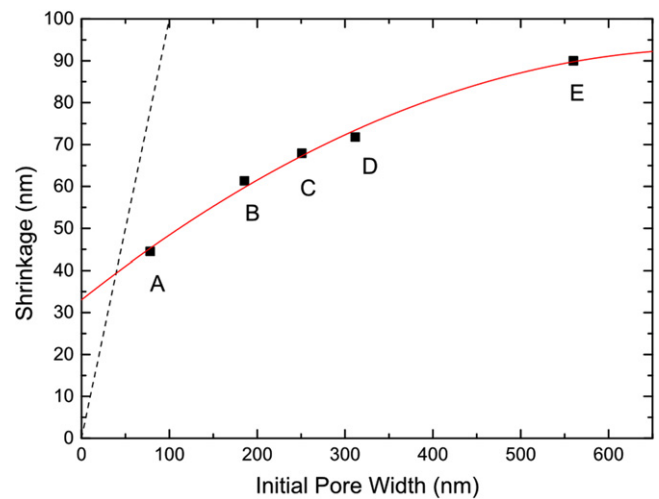


Figure 4. Pore width shrinkage versus initial pore width after 4 h of oxidation. In addition to the four pore sizes (A, B, C, and D) data point E is shown, which is the average value from pores defined by optical lithography. The solid red line is a guide to the eye. The dashed black line indicates the case when shrinkage is equal to the initial pore width and thus results in a closed pore. The larger the initial opening is, the greater the shrinkage becomes. This can be explained by the stress-related retardation of the oxidation for non-planar silicon structures.

pyramidal shape, concave and convex structures exist at the same time: from the top view, the corners of square pores have large negative curvatures, while from a cross-sectional view the bottom edges (O) of the inner pore walls have a large positive curvature. For smaller concave pores, the compressive stress which built up during oxidation is larger than that for larger pores. But the tensile stresses at the bottom edges of the inner pore wall are the same regardless of the pore size, since the angle of the inverted pyramids is the same for all openings, 54.7°. Therefore, the compressive and tensile stresses compensate for each other to some extent at the pore walls. The experimental results suggest that the compressive stress dominates at the pore walls, resulting in thinner oxide in the smaller pores and thicker oxide in the larger ones. When the

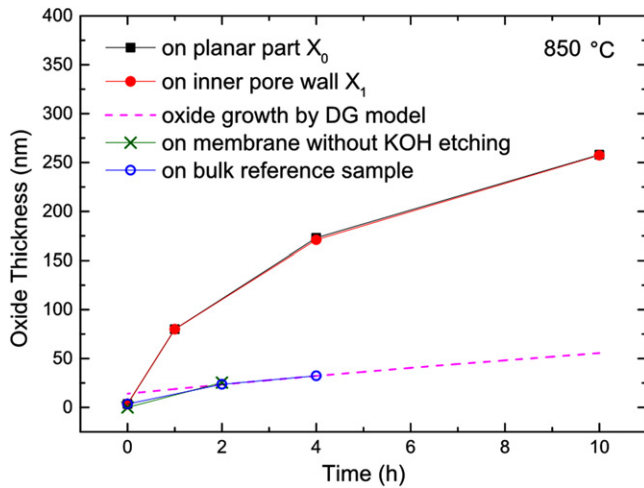


Figure 5. The oxide growth at the planar part of the membrane and on the pore walls' part continues with oxidation time. The thickness of the oxide on planar part (X_0) and the inner pore walls (X_1) are almost the same for pores in group E, so that the red circular data points overlap with the black square data points. The oxidation rate on the nanopore membrane is faster than that on a membrane sample without KOH etching, probably due to potassium impurities in the membrane.

thickness of the oxide on the pore walls is less, there would be less oxide participating in oxide deformation, leading to a reduced shrinkage rate of the pore diameter. Hence, the shrinkage rate of the pore is proportional to the initial pore size, as experimental data indeed confirm in figure 4. In other words, smaller pores shrink less, which can also explain the narrowing of the distribution of pore widths under progressing oxidation. It is important to keep this fact in mind when scaling nanopores down to the single-nanometer range. Another observation is that within one pore, the remaining silicon cores kept almost the same angle as the initial 54.7° . In fact, the oxidation is even slightly faster at the upper and bottom edges, as can be seen in figure 3. It may be the case that the tensile stress at these edges is partly cancelled or even completely compensated by the compressive stress, which is introduced by the concave pore structure, creating a low stress region around the edges. Hence, the oxidation is faster around the edges. A dedicated simulation of oxidation on such a complex 3D silicon structure is required for a more clarified explanation of these experimental results. However, it is beyond this paper's scope.

Further, to explain the saturation of the shrinkage, it is first tempting to use the theory of stress-related oxidation, implying that the oxidation at the bottom edge of the pore is hindered by the stress induced by the non-planar nanostructure. However, this is less likely the case, since the bottom edges of the pore actually have a slightly faster oxidation rate as discussed previously. Moreover, the oxide on both the planar part on the membrane (X_0) and on the inner pore walls (X_1) continues to grow after the shrinkage saturated after 4 h of oxidation (see figure 5). We believe that the saturation of the shrinkage is mainly attributed to the pyramidal pore geometry. The deformation of the oxide on such inverted pyramidal structures is

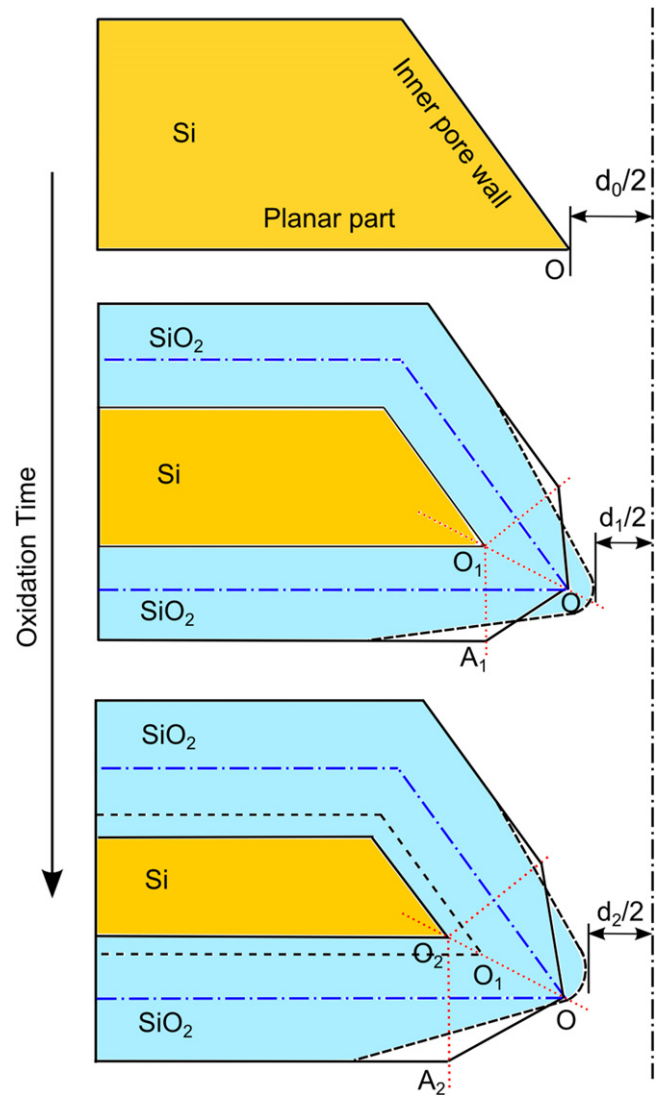


Figure 6. Schematic cross-sectional illustration showing the oxidation progression with particular focus at the bottom edge of the pyramidal opening. The oxidation can be divided into two steps for simplicity: volume expansion when Si converts into SiO_2 (illustrated by solid black line) and oxide deformation to relax stress and achieve a lower surface energy (illustrated by dashed black line). Deformed oxide at the bottom edge (O) induces the pore shrinkage. With oxidation time, as the bottom edge of the remaining silicon core withdraws, so does the frontier of the newly grown oxide (A_n), which hardly influences the deformation at the bottom edge (O). Pore shrinkage is then saturated. When oxidation progresses, the oxide on the planar part pushes the bottle neck of the pore upwards, resulting in a slight increase in pore diameter.

limited at low oxidation temperatures (here 850°C). To understand the influence of the initial pore geometry on the observed oxidation behavior, the progression of oxidation is illustrated in figure 6. The schemes are based on cross-sectional images obtained from the oxidized pores (for example figure 3). The half width of the silicon pore is $d_0/2$ before the oxidation. As the oxidation goes on, the newly grown oxide pushes out the old oxide, forcing it to rearrange at the pore bottom edge (O) in order to relax stress and achieve a lower surface energy. The oxide sticks out of the original narrowest point of the pore, thus

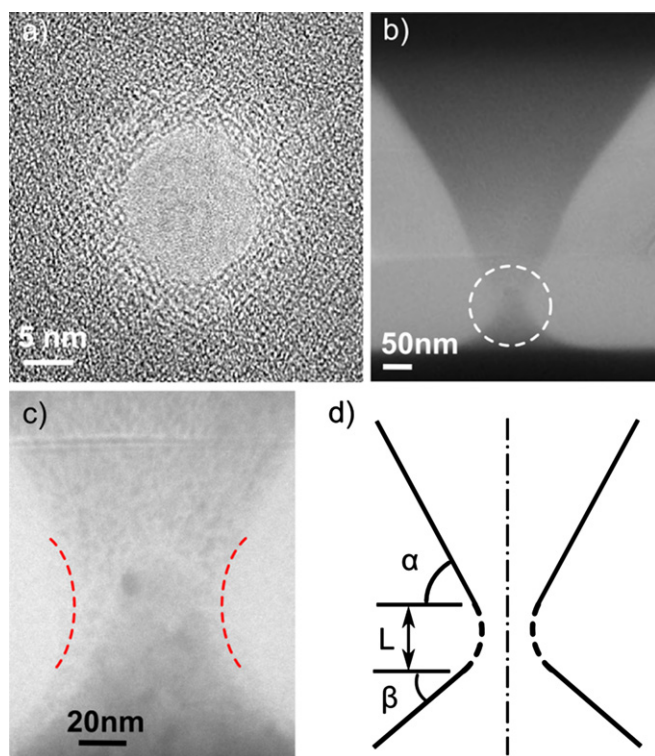


Figure 7. TEM images showing the top view and the cross-sectional views of FIB-cut oxidized nanopores. (a) Top view of a circular nanopore with a diameter of 13 nm after 10 h oxidation. (b) Cross-sectional view of a nanopore with a diameter of 69 nm after 3 h of oxidation. (c) Zoomed-in image of the bottleneck of the pore shown in (b). (d) A cross-sectional scheme of a nanopore that has been shrunk by thermal oxidation.

the pore width/radius reduces to $d_1/2$. Meanwhile, as the bottom edge of the pore (O_n) withdraws from the original position (O), so does the frontier of the newly grown oxide (A_n). Since oxide has a rather high viscosity at 850 °C, the extent of the oxide deformation is limited. The further the frontier of the newly grown oxide withdraws, the less it contributes to the oxide deformation at the bottom edge of the pore. Therefore, the shrinkage rate of the pore slows down significantly in the beginning of the oxidation. After about 4 h the newly grown oxide has limited influence on pushing oxide to the bottom edges, effectively saturating the shrinkage rate. As the oxidation goes on, the oxide continuously grows while the silicon core shrinks. The ratio of the length of the planar part to the inner pore wall part increases from 6:1 to 13:1 after 10 h of oxidation. The increasing volume difference of the oxide grown on the planar part and on the inner pore wall part causes the bottleneck of the pore to be pushed towards the inner pore wall part. Since the actual amount of the oxide around the bottleneck is not changing, as the bottleneck shifts its ‘nose’ up, the half width/radius of the pore enlarges to $d_2/2$. The upward shift of the bottleneck can be also seen in figure 3(b) and the slight increase of the pore widths/radius in figure 2(a). This means that the pore size can be finely tuned to be decreased or even enlarged, simply by adjusting the oxidation time within the saturation regime. Note that the oxide growth on the KOH-etched nanopore membrane is much faster than that on the non-KOH-

etched membrane sample, bulk reference sample and the prediction by the Deal–Grove model at 850 °C [30], also shown in figure 5. The possibility of a local temperature increase on the nanopore membrane was ruled out after a careful calculation of the heat release rate during the oxidation process and a simulation of the heat transfer on a porous Si membrane with poor thermal conductivity. The most probable explanation is that potassium impurities, introduced by the KOH etching step, accelerated the oxidation reaction rate and the oxidant diffusion rate [31]. A further experiment, where KOH is replaced by tetramethylammonium hydroxide (TMAH) to form the initial pyramidal pores, is planned to investigate the cause of the abnormal oxidation rate.

Finally, we focused on the smallest nanopores from group A to determine the 3D structure of the nanopores by FIB and TEM. Top view TEM images of the oxidized nanopores in group A confirmed the observations seen in SEM. Pores with diameters less than 110 nm display a circular shape after oxidation. A typical top view of a nanopore with a diameter of 13 nm is shown in figure 7(a), while a cross-sectional view of a pore with a diameter of 69 nm is shown in figure 7(b). In figure 7(c), a zoomed-in image of the pore is shown, in which the white area is the oxide and the darker area is the part of the pore coated with platinum. Oxidation of the truncated pyramidal structure results in an hourglass-shaped nanopore with smooth arcs (red dashed line in (c) and black dashed line in (d)) forming the bottleneck of the nanopore. The ‘hourglass’ is not symmetric along the y -axis because of the initial truncated pyramidal structure. For pores after 10 h of oxidation, the upper part of the ‘hourglass’ has a length of about 450 nm with an angle $\alpha = 63.9^\circ \pm 0.9^\circ$, while the lower part is within 100 nm with an angle $\beta = 43.4^\circ \pm 7.7^\circ$. The bottleneck length L is approximately between 30–70 nm. Within the length L , the diameter of the pore varies within 10% of the diameter at the narrowest point. The asymmetric structure of the oxidized pores is particularly interesting for various molecular sensing applications, due to its unique ion transport properties [10, 11]. In addition, with the relatively high aspect ratio of the pore (membrane thickness to bottleneck diameter), which would lower the electric field strength when an electric bias is applied across the membrane in a buffer solution, the velocity of a molecule passing through a nanopore would be slower. Hence, a better temporal resolution could be achieved during biomolecular sensing/sequencing [3, 13].

Conclusion

We have demonstrated that silicon nanopores as small as 8 nm can be fabricated by a one-step low-temperature oxidation of inverted pyramidal pores. The shrinkage of inverted pyramidal pores with different sizes in a silicon membrane was studied using dry thermal oxidation at 850 °C. An important observation is that the shrinkage of pores with initial width over a range from several tens of nanometers to hundreds of nanometers shows similar self-limiting behavior. Rectangular pores with widths less than 110 nm transformed

into perfect circular pores after oxidation. TEM cross sections of pores indicate that a stress-related retardation of oxidation causes slight differences in the shrinkage of the pores with different initial size. However, the self-limiting behavior of the pore shrinkage is more likely due to the pyramidal geometry of the pores, since the oxide growth on the pore walls and at the planar part of the membrane were both continuously increasing after pore shrinkage already stopped. Further, statistical analysis suggests that no process-induced size variation was added by the oxidation. The distribution of the pore width even slightly decreased in most cases, possibly as a result of the self-limiting shrinking effect. An initially narrow distribution of the pore openings is crucial for future successful mass fabrication of large arrays of nanopores, which can be applied in high throughput parallel DNA sequencing as well as for single molecule detection.

Acknowledgment

This project is funded by the Swedish Foundation for Strategic Research.

References

- [1] Deamer D W and Akeson M 2000 Nanopores and nucleic acids: prospects for ultrarapid sequencing *Trends Biotechnol.* **18** 147–51
- [2] Kasianowicz J J, Brandin E, Branton D and Deamer D W 1996 Characterization of individual polynucleotide molecules using a membrane channel *Proc. Natl Acad. Sci. USA* **93** 13770–3
- [3] Chansin G A T, Mulero R, Hong J, Kim M J, DeMello A J and Edel J B 2007 Single-molecule spectroscopy using nanoporous membranes *Nano Lett.* **7** 2901–6
- [4] Kannam S K, Kim S C, Rogers P R, Gunn N, Wagner J, Harrer S and Downton M T 2014 Sensing of protein molecules through nanopores: a molecular dynamics study *Nanotechnology* **25** 155502
- [5] Wanunu M, Sutin J and Meller A 2009 DNA profiling using solid-state nanopores: detection of DNA-binding molecules *Nano Lett.* **9** 3498–502
- [6] McNally B, Singer A, Yu Z, Sun Y, Weng Z and Meller A 2010 Optical recognition of converted DNA nucleotides for single-molecule DNA sequencing using nanopore arrays *Nano Lett.* **10** 2237–44
- [7] Miles B N, Ivanov A P, Wilson K A, Doğan F, Japrun D and Edel J B 2013 Single molecule sensing with solid-state nanopores: novel materials, methods, and applications *Chem. Soc. Rev.* **42** 15–28
- [8] Li J, Stein D, McMullan C, Branton D, Aziz M J and Golovchenko J A 2001 Ion-beam sculpting at nanometre length scales *Nature* **412** 166–9
- [9] Storm A J, Chen J H, Ling X S, Zandbergen H W and Dekker C 2003 Fabrication of solid-state nanopores with single-nanometre precision *Nat. Mater.* **2** 537–40
- [10] Kim M J, Wanunu M, Bell D C and Meller A 2006 Rapid fabrication of uniformly sized nanopores and nanopore arrays for parallel DNA analysis *Adv. Mater.* **18** 3149–53
- [11] Wu M-Y, Smeets R M M, Zandbergen M, Ziese U, Krapf D, Batson P E, Dekker N H, Dekker C and Zandbergen H W 2009 Control of shape and material composition of solid-state nanopores *Nano Lett.* **9** 479–84
- [12] Park S R, Peng H and Ling X S 2007 Fabrication of nanopores in silicon chips using feedback chemical etching *Small* **3** 116–9
- [13] Mara A, Siwy Z, Trautmann C, Wan J and Kamme F 2004 An asymmetric polymer nanopore for single molecule detection *Nano Lett.* **4** 497–501
- [14] Moon J-M, Akin D, Xuan Y, Ye P D, Guo P and Bashir R 2009 Capture and alignment of phi29 viral particles in sub-40 nanometer porous alumina membranes *Biomed. Microdevices* **11** 135–42
- [15] Létant S E, Buuren T W V and Terminello L J 2004 Nanochannel arrays on silicon platforms by electrochemistry *Nano Lett.* **4** 1705–7
- [16] Kumar R T R, Badel X, Vikor G, Linnros J and Schuch R 2005 Fabrication of silicon dioxide nanocapillary arrays for guiding highly charged ions *Nanotechnology* **16** 1697–700
- [17] Deng T, Chen J, Li M, Wang Y, Zhao C, Zhang Z and Liu Z 2013 Controllable shrinking of inverted-pyramid silicon nanopore arrays by dry-oxygen oxidation *Nanotechnology* **24** 505303
- [18] Liu H I, Biegelsen D K, Ponce F A, Johnson N M and Pease R F W 1994 Self-limiting oxidation for fabricating sub-5 nm silicon nanowires *Appl. Phys. Lett.* **64** 1383
- [19] Liu H I 1993 Self-limiting oxidation of Si nanowires *J. Vac. Sci. Technol. B Microelectron. Nanom. Struct.* **11** 2532
- [20] Sychugov I, Juhasz R, Valenta J, Zhang M, Pirouz P and Linnros J 2006 Light emission from silicon nanocrystals: probing a single quantum dot *Appl. Surf. Sci.* **252** 5249–53
- [21] Prins F E, Single C, Zhou F, Heidemeyer H, Kern D P and Piles E 1999 Thermal oxidation of silicon-on-insulator dots *Nanotechnology* **132** 132–4
- [22] Bruhn B, Valenta J and Linnros J 2009 Controlled fabrication of individual silicon quantum rods yielding high intensity, polarized light emission *Nanotechnology* **20** 505301
- [23] Takahashi Y, Nagase M, Namatsu H, Kurihara K, Iwade K, Nakajima S, Horiguchi S, Murase K and Tabe M 1995 Fabrication technique for Si single-electron-transistor operating at room temperature *Electron. Lett.* **31** 136–7
- [24] Kao D-B, McVittie J P, Nix W D and Saraswat K C 1987 Two-dimensional thermal oxidation of silicon—I. Experiments *IEEE Trans. Electron Devices* **34** 1008–17
- [25] Krzeminski C D, Han X-L and Larrieu G 2012 Understanding of the retarded oxidation effects in silicon nanostructures *Appl. Phys. Lett.* **100** 263111
- [26] Senez V, Collard D, Baccus B, Brault M and Lebailly J 1994 Analysis and application of a viscoelastic model for silicon oxidation *J. Appl. Phys.* **76** 3285
- [27] Sutardja P and Oldham W G 1989 Modeling of stress effects in silicon oxidation *IEEE Trans. Electron Devices* **36** 2415–21
- [28] Uematsu M, Kageshima H, Shiraishi K, Nagase M, Horiguchi S and Takahashi Y 2004 Two-dimensional simulation of pattern-dependent oxidation of silicon nanostructures on silicon-on-insulator substrates *Solid State Electron.* **48** 1073–8
- [29] Kao D-B, McVittie J P, Nix W D and Saraswat K C 1988 Two-dimensional thermal oxidation of silicon. II. Modeling stress effects in wet oxides—electron devices *IEEE Trans. Electron Devices* **35** 25–37
- [30] Deal B E and Grove A S 1965 General relationship for the thermal oxidation of silicon *J. Appl. Phys.* **36** 3770
- [31] Revesz A G and Evans R J 1969 Kinetics and mechanism of thermal oxidation of silicon with special emphasis on impurity effects *J. Phys. Chem. Solids* **30** 551–64